



Evidence for complex iron oxides in the deep mantle from FeNi(Cu) inclusions in superdeep diamond

Chiara Anzolini^{a,b,1}, Katharina Marquardt^{c,2}, Vincenzo Stagno^{d,e}, Luca Bindf^f, Daniel J. Frost^g, D. Graham Pearson^b, Jeffrey W. Harris^g, Russell J. Hemley^{h,i,1}, and Fabrizio Nestola^a

^aDepartment of Geosciences, University of Padova, I-35131 Padova, Italy; ^bDepartment of Earth and Atmospheric Sciences, University of Alberta, T6G 2E3 Edmonton, Canada; ^cBayerisches Geoinstitut, University of Bayreuth, D-95440 Bayreuth, Germany; ^dDepartment of Earth Sciences, Sapienza University of Rome, I-00185 Rome, Italy; ^eNational Institute of Geophysics and Volcanology, Rome Headquarters, 00143 Roma, Italy; ^fDepartment of Earth Sciences, University of Firenze, I-50121 Firenze, Italy; ^gSchool of Geographical and Earth Sciences, University of Glasgow, G12 8QQ Glasgow, United Kingdom; ^hDepartment of Physics, University of Illinois at Chicago, Chicago, IL 60607; and ⁱDepartment of Chemistry, University of Illinois at Chicago, Chicago, IL 60607

Contributed by Russell J. Hemley, June 19, 2020 (sent for review March 6, 2020; reviewed by Daniele Antonangeli, Kenneth Collerson, and Arno Rohrbach)

The recent discovery in high-pressure experiments of compounds stable to 24–26 GPa with Fe₄O₅, Fe₅O₆, Fe₇O₉, and Fe₉O₁₁ stoichiometry has raised questions about their existence within the Earth's mantle. Incorporating both ferric and ferrous iron in their structures, these oxides if present within the Earth could also provide insight into diamond-forming processes at depth in the planet. Here we report the discovery of metallic particles, dominantly of FeNi (Fe_{0.71}Ni_{0.24}Cu_{0.05}), in close spatial relation with nearly pure magnetite grains from a so-called superdeep diamond from the Earth's mantle. The microstructural relation of magnetite within a ferropicrlase (Mg_{0.60}Fe_{0.40}O) matrix suggests exsolution of the former. Taking into account the bulk chemistry reconstructed from the FeNi(Cu) alloy, we propose that it formed by decomposition of a complex metal *M* oxide (M₄O₅) with a stoichiometry of (Fe³⁺_{2.15}Fe²⁺_{1.59}Ni²⁺_{0.17}Cu⁺_{0.04})_Σ = 3.95O₅. We further suggest a possible link between this phase and variably oxidized ferropicrlase that is commonly trapped in superdeep diamond. The observation of FeNi(Cu) metal in relation to magnetite exsolved from ferropicrlase is interpreted as arising from a multistage process that starts from diamond encapsulation of ferropicrlase followed by decompression and cooling under oxidized conditions, leading to the formation of complex oxides such as Fe₄O₅ that subsequently decompose at shallower *P-T* conditions.

oxidized fluids (6, 11–13). Such observations suggest a mantle redox state varying between reduced conditions, where metallic Fe and diamond can occur together [*f*₀₂ ~ iron-wüstite (IW) buffer (10)], and more oxidized conditions that allow the coexistence of diamond and carbonates [either solid or liquid; *f*₀₂ ~ IW > + 2 log units (12, 14, 15)].

Investigations to date of Mg–Fe oxides trapped in SDDs have revealed a diverse suite of minerals that can be summarized by the MgO–FeO–Fe₂O₃ ternary diagram, with ferropicrlase being the most abundant phase. Ferropicrlase inclusions are the most abundant inclusions in SDDs and account for 50–56% of all identified lower-mantle inclusions (13), despite the fact that constraints obtained from computational studies to date indicate that ferropicrlase should only comprise ~17% of the lower mantle (16). Ferropicrlase inclusions have been linked to the presence of Fe metal in the deep mantle. However, their wide range in Fe# suggests either local chemical heterogeneities (17, 18) or kinetically controlled chemical (redox) reactions that promote the encapsulation of ferropicrlase during diamond formation (6, 19–21). Ref. 18 first identified magnesioferrite

diamond inclusions | mantle dynamics | iron oxides | Earth's deep interior | Fe–Ni alloys

Sublithospheric diamond is an exceptionally rare category of diamond, representing ~1% of the total abundance (1), that crystallized at depths between ~300 km and perhaps greater than ~1,000 km (2–5). Also called superdeep diamond (SDD), these are distinguished from more common lithospheric diamond that forms in shallower regions between ~120- and ~250-km depth (1). In the last decade, these extraordinary diamond samples and their mineral and fluid inclusions have yielded new insights into the interior of our planet (2–9). Although this class of diamond can trap fragments of deep Earth materials, it remains uncertain whether trapped minerals represent surrounding rocks and reflect the local mantle pressure–temperature–oxygen fugacity (*P-T-f*₀₂) conditions. Slivers of metallic iron–nickel and iron carbides surrounded by reducing gases (CH₄ and H₂) in unusually large SDD crystals have been recently reported (4). This finding was interpreted as evidence for their growth from liquid metal within highly reducing deep-mantle regions between ~300- and ~1,000-km depth. Further, the observation represents the first natural evidence of a process that was previously only observed in high-pressure experiments on the relevant minerals at conditions of deep-mantle saturation by an Fe(Ni) metal phase (10). A similar conclusion has been reached for boron-bearing SDD crystals sampled from several localities around the world (7). In contrast, experimental studies as well as geophysical and geochemical evidence confirm that inclusions of CO₂-bearing minerals and melts provide strong support of the passage of

Significance

Diamonds are among the most important samples of the solid Earth owing to the unique information they provide about the planet's interior. New analytical techniques have enabled the discovery of distinct inclusions in diamond hosts having mineral associations that constrain the mineralogy at great depths within the Earth. Currently, experimental studies are revealing the stability of novel iron oxides not found at Earth's surface but that would be present in the mantle. We combine textural and chemical analyses on ferropicrlase inclusions contained in a diamond sample and demonstrate that the observed association of magnetite + FeNi metal exsolved from the matrix results from postentrapment decomposition at the expense of a natural Fe₄O₅ phase recently discovered and characterized in high-pressure experiments.

Author contributions: F.N. designed research; C.A., K.M., and F.N. performed research; C.A., K.M., D.G.P., J.W.H., and F.N. contributed new reagents/analytic tools; C.A., K.M., V.S., L.B., and F.N. analyzed data; and C.A., K.M., V.S., L.B., D.J.F., D.G.P., J.W.H., R.J.H., and F.N. wrote the paper.

Reviewers: D.A., Sorbonne University; K.C., The University of Queensland; and A.R., University of Münster.

The authors declare no competing interest.

Published under the PNAS license.

¹To whom correspondence may be addressed. Email: anzolini@ualberta.ca and rhemley@uic.edu.

²Present address: Department of Materials, Imperial College London, SW7 2AZ London, United Kingdom.

This article contains supporting information online at <https://www.pnas.org/lookup/suppl/doi:10.1073/pnas.2004269117/-DCSupplemental>.

First published August 12, 2020.

exsolved from ferropericlyase, then confirmed in a number of studies (20, 22–25), and estimated it to be 6–7 vol % of the original mineral. A similar estimate has been made on the same sample examined in the present study (26). Nanometer-scale investigations using transmission electron microscopy (TEM) revealed the presence of magnesioferrite within an $(\text{Fe}_{0.65}\text{Mg}_{0.35})\text{O}$ magnesio-wüstite included in an SDD (22). These authors stated that magnesioferrite comprised ~5–7% of a wüstite component and precipitated either on dislocations or at the interface with diamond. In the same work, blebs of FeNi and rare 20–50-nm-sized magnetite exsolutions were also reported. The presence of a small amount of Cu was also detected in Fe–Ni, although it was attributed to secondary X-rays from the copper TEM grid (22).

Magnesioferrite has also been observed along with carbonated mineral assemblages, indicating the important role of high- f_{O_2} conditions on the initial bulk Fe^{3+} content (27). Spinel exsolutions in $(\text{Mg}_{0.83}\text{Fe}_{0.17})\text{O}$ ferropericlyase such as magnesioferrite that are relatively enriched in Cr and Al have been reported (24). The observed epitaxial growth relationships with ferropericlyase suggested these spinel inclusions had exsolved from the matrix where nucleation was facilitated at dislocations (24), in agreement with refs. 18 and 22. Consistent with the observations for SDD ferropericlyase inclusions, experiments showing the formation of magnesioferrite on decomposition of Fe^{3+} -rich bridgmanite at 24 GPa have been explained as a consequence of saturation in ferric iron due to decompression (28). The formation of magnesioferrite thus appears to be related to the abundance of Fe^{3+} in the matrix. Finally, experimental studies of the synthesis of ferropericlyase focused on the formation of magnesioferrite as an exsolution product due to either an increase in the f_{O_2} of annealing or the effect of cooling have been reported (ref. 29 and references therein).

Recent experiments performed at temperatures between ~1,500 and ~2,000 K and pressures from 8 to 22 GPa have succeeded in synthesizing several new mixed-valence Fe-oxides with various stoichiometries along the FeO – Fe_3O_4 join (30, 31), such as the orthorhombic-structured phases Fe_4O_5 (30) and Fe_5O_6 (32), and the monoclinic-structured phases Fe_7O_9 (33) and Fe_9O_{11} (34). The finding of these new compounds raised the possibility that several iron oxides with different stoichiometries may be stable at conditions corresponding to the deep Earth's mantle. Interestingly, Fe_4O_5 and Fe_5O_6 have been both shown to form solid solutions with Mg and Cr counterparts and to coexist with silicate phases at the high- P - T conditions expected in the transition zone of the mantle, including wadsleyite and ringwoodite (35). In addition, these phases can incorporate Fe^{3+} in their structure, implying therefore a role in redox-driven processes such as diamond formation. The oxygen fugacity (f_{O_2}) is a key variable affecting the stability of carbon, for instance, either as diamond or carbonate (solid or melt). Whether these oxide phases can locally buffer the f_{O_2} in the deep mantle will depend on the effect that Fe^{3+} has on their stability. Experimental studies supported by thermodynamic calculations have shown that Fe_4O_5 and Fe_5O_6 can be stable at redox conditions where carbonate and diamond, respectively, are stable along with the more abundant silicate minerals (36, 37). However, to date, no diamond samples have shown evidence of the presence of Fe_xO_y minerals trapped as inclusions.

Here we report the direct observation of FeNi(Cu) metallic particles in close spatial relation with nearly pure magnetite grains trapped in two $(\text{Mg}_{0.60}\text{Fe}_{0.40})\text{O}$ ferropericlyase inclusions within an SDD. Textural and chemical analyses combined with the reconstructed bulk chemistry provide a clear evidence of decomposition of complex metal Fe–O oxides.

Results

The $(\text{Mg}_{0.60}\text{Fe}_{0.40})\text{O}$ ferropericlyase inclusions from an SDD from Juina, Mato Grosso State, Brazil (Fig. 1A) were examined. The diamond crystallized at a minimum calculated pressure of 15.7

(± 2.5) GPa at 1,830 (± 45) K (26), and contains exsolutions of magnetite (~400 nm); these in turn show metallic FeNi particles (50–200 nm), with minor amounts of Cu. The two inclusions (AZ1_1 and AZ1_2) were identified by single-crystal X-ray diffraction and electron microprobe analyses (EMPA) as ferropericlyase. The two inclusions appear identical in terms of chemistry and texture. Indeed, the polished surface of both inclusions exhibits pervasive, homogeneously distributed nanometer-sized exsolutions of magnetite (with negligible amounts of Al and Mg), which represents ~6% of the total area (SI Appendix, Fig. S1); see *Materials and Methods* below. These exsolutions were initially identified as magnesioferrite (26) but after transmission electron microscopy - energy dispersive X-ray spectroscopy (TEM-EDS) analyses were performed, they were revealed to be pure magnetite (Fig. 2 and SI Appendix, Fig. S2). The average size of the magnetite exsolutions is ~400 nm and they often coalesce in chains of 2–3- μm length (Fig. 2). Preliminary analyses provided a composition of $(\text{Mg}_{0.61}\text{Fe}_{0.39})\text{O}$ for inclusion AZ1_1 and $(\text{Mg}_{0.59}\text{Fe}_{0.41})\text{O}$ for AZ1_2. Due to the identical microstructure and chemistry of the two inclusions, ref. 26 focused on inclusion AZ1_1 only, for which these authors determined the minimum entrapment pressure by elastoplastic geobarometry. Chemical analyses were carried out on the inclusion (39 spots, *Materials and Methods*). The average chemical composition of ferropericlyase was confirmed to be very close to that determined by FEG-SEM, i.e., $(\text{Mg}_{0.580}\text{Fe}_{0.412})\text{O}$, with minor amounts of Mn (0.003 per formula unit [p.f.u.]), Ni (0.003 p.f.u.), and Cr (0.001 p.f.u.) (SI Appendix, Table S1). Si, Al, Na, Ti, and Cu were below the detection limit. We can approximate the composition of the AZ1_1 inclusion as $(\text{Mg}_{0.60}\text{Fe}_{0.40})\text{O}$.

Both field emission gun-scanning electron microscopy (FEG-SEM) and high-angle annular dark-field-scanning transmission electron microscopy (HAADF-STEM) investigations using Z-contrast imaging parameters revealed that, besides the spinel-structured grains, small particles have a brighter contrast than magnetite, implying enrichment in heavier elements (Fig. 2). The first two electron-transparent lamellae, cut using the focused ion beam (FIB) technique, were placed on Cu grids (SI Appendix, Fig. S1), providing an explanation of the high Cu content in the first analyzed Ni-bearing particles. To prevent a Cu signal produced by secondary excitation of the grid, the third lamella (AZ1_1B) was mounted on a Mo grid (Fig. 3) and its analysis confirmed the presence of Cu in the particles. Bright-field images combined with TEM-EDS element distribution of AZ1_1B are presented in Fig. 3. A bright-field image of a portion of the ferropericlyase inclusion containing different types of exsolutions is shown in Fig. 3A, whereas Fig. 3B–D and H details the element distribution for Fe, Mg, Cu, Cr, Al, O, and Ni, respectively. On the right side of the same figure, three EDS spectra of ferropericlyase (green), magnetite (red), and the third phase, which is an FeNi(Cu) alloy (blue), are shown. The HAADF-STEM image of magnetite trapped in ferropericlyase is morphologically similar (Fig. 2) to the “pearl necklaces” of magnesioferrite described in refs. 22 and 24. Furthermore, the bright blebs, whose dimensions are about 5 nm \times 80 nm, are composed of Fe and Ni with minor Cu, while O is absent (Fig. 3). The absence of oxygen implies a metallic nature of the FeNi particles. These contain variable minor amounts of Cu, and traces of Al and Cr, as indicated in the TEM compositional maps (Fig. 3). The average composition of the metallic particles—neglecting Al and Cr due to their very low concentrations and basing on the EDS spectra measured on the lamella mounted on molybdenum—is $\text{Fe}_{0.71}\text{Ni}_{0.24}\text{Cu}_{0.05}$.

Fig. 4 shows the electron diffraction patterns and high-resolution TEM images obtained on all three phases presented in Fig. 2. The figure provides an overview of the orientation relationships between the ferropericlyase matrix, magnetite grains, and FeNi(Cu) particles. The bright-field image shows the

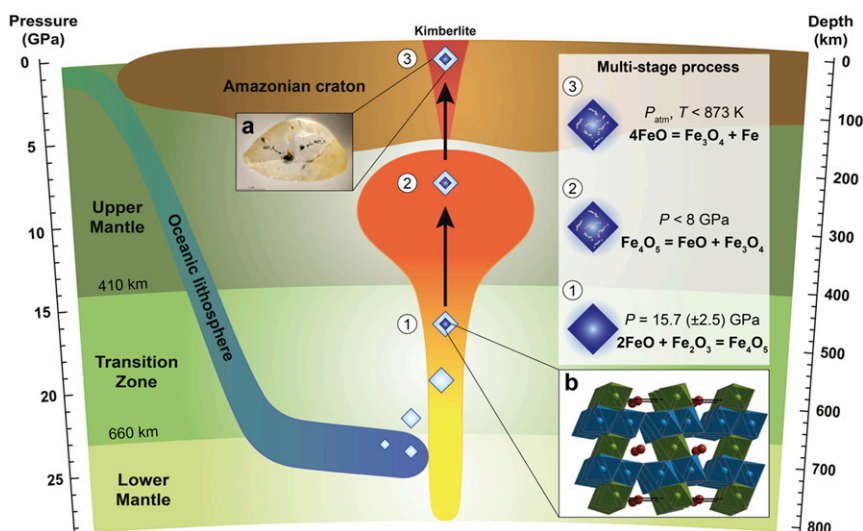


Fig. 1. Schematic of FeNi(Cu) inclusions formation through a multistage process during diamond exhumation: 1) at 15.7 (± 2.5) GPa Fe_4O_5 exsolves from FeO as the Fe^{3+} solubility is exceeded due to decompression; 2) below 8 GPa Fe_4O_5 decomposes to almost-pure wüstite and magnetite; 3) at room pressure $P = 0.1$ MPa and $T < 873$ K wüstite becomes unstable and FeNi(Cu) metal alloy forms. (A) Photograph of the inclusion-bearing diamond studied in this work (the longest dimension is 4 mm, ref. 26). (B) Crystal structure of Fe_4O_5 viewed along the a axis (from ref. 30), where green and blue octahedra represent sites Fe1 and Fe2, respectively, whereas red spheres represent site Fe3.

distribution of magnetite in ferropericlasite (Fig. 4A). Magnetite exsolution often align along trails or chains. Fig. 4B shows a high-resolution TEM image of ferropericlasite and magnetite; their diffraction pattern is displayed in Fig. 4C. The pattern shows clear topotaxy with $\langle 111 \rangle_{\text{magnetite}}$ coincident with $\langle 111 \rangle_{\text{ferropericlasite}}$. Fig. 4D shows a region where the three phases are coexisting together. Finally, Fig. 4 E, G, and H show the Fourier transformations of the indicated regions, while Fig. 4F shows a selected area diffraction pattern of the whole region, confirming that the identified phases are ferropericlasite, magnetite, and FeNi(Cu) alloy. The best indexing match of the FeNi(Cu) alloy TEM diffraction pattern provides a cubic symmetry with unit-cell parameter $a = 3.617 \text{ \AA}$, which corresponds to a volume $V = 47.32 \text{ \AA}^3$. The additional diffraction peaks, that belong neither to ferropericlasite nor to magnetite, and are not the direct diffraction peak of FeNi(Cu), arise due to double diffraction in the small-sized FeNi(Cu) and magnetite particles. Double diffraction is typical in epitaxial multiphase systems. The streaks in the $(1\bar{1}1)$ reciprocal direction at the 002 FeNi(Cu) reflection indicate that the particle is faceted, thus it is little extended perpendicular to the $(1\bar{1}1)$ plane. Generally, our diffraction and imaging work indicates that the particles shapes are defined by well-developed $\{111\}$ planes with minor development of the $\{100\}$ planes. Although we cannot exclude twinning in the FeNi(Cu) particle reported in Fig. 4—twinning was indeed observed in some FeNi(Cu) particles as well as in magnetite (SI Appendix, Figs. S3 and S4)—we prefer the simplest possible solution (i.e., “double diffraction”) to explain our observations.

Discussion

Recent experimental studies have led to the discovery of new crystalline phases with Fe_xO_y stoichiometry, stable over a wide range in P - T - f_{O_2} space, whose stability during decompression as well as their potential existence within the Earth are not yet proven. Theoretical considerations and experimental evidence indicates FeNi metal saturation below 250 (± 30) km (10, 38–41) as a result of the decreasing f_{O_2} with depth and pressure effects leading to the disproportionation reaction at the expense of Fe^{2+} to form Fe^{3+} -bearing minerals + Fe(Ni) alloy (42). Experimental studies show that the ferropericlasite equilibrated with Fe

metal has an Fe/(Fe+Mg) (Fe#) of ~ 0.20 and NiO contents of ~ 0.5 wt % (43). In contrast, the ferropericlasite inclusion studied here has a Fe# of 0.41 and contains 0.4 wt % NiO. This composition is in good agreement with the worldwide composition of ferropericlasite inclusions such as those from Guaniamo (Venezuela), but differs from the predicted primordial composition (43). This variation might indicate that ferropericlasite is not equilibrated at mantle conditions; rather, it crystallized upon decompression from a different precursor, prior to or simultaneously with entrapment in the diamond host (20). We therefore suspect that the presence of magnetite trapped in ferropericlasite can have a direct link with the local mineralogy and redox state of the deep mantle. We suggest that a series of exsolution reactions is required to explain the presence of magnetite and FeNi alloy from ferropericlasite.

Further, assuming a pure Fe_3O_4 composition for magnetite (as only negligible Mg and Al were detected by TEM-EDS; see Fig. 2 and SI Appendix, Fig. S2), a normalized composition for the FeNi(Cu) alloy of $\text{Fe}_{0.71}\text{Ni}_{0.24}\text{Cu}_{0.05}$ (the composition of the alloy particles measured by TEM using a Mo grid) and a magnetite:metal ratio of $\sim 6:1$ (as measured from both FEG-SEM and TEM images), we can reconstruct the bulk chemistry of the precursor. The result is a phase with stoichiometry of either $(\text{Fe}^{3+}_{2.15}\text{Fe}^{2+}_{1.59}\text{Ni}^{2+}_{0.17}\text{Cu}^{+}_{0.04})_{\Sigma} = 3.95\text{O}_5$ (using a basis of five oxygen atoms), or $(\text{Fe}^{3+}_{2.57}\text{Fe}^{2+}_{1.91}\text{Ni}^{2+}_{0.21}\text{Cu}^{+}_{0.04})_{\Sigma} = 4.73\text{O}_6$ (using a basis of six oxygen atoms). From this analysis and based on charge, it is evident that the Fe_4O_5 phase is favored relative to Fe_5O_6 as the ideal stoichiometry. However, given the uncertainties, both Fe_4O_5 and Fe_5O_6 are potential candidates to explain the exsolution from ferropericlasite that ultimately decomposed to an assemblage of magnetite + FeNi(Cu) metal. A similar equally valid calculation could also be performed for the recently discovered Fe_7O_9 phase, which is very close to Fe_4O_5 in stoichiometry, but given the limited information concerning its stability field (33) we do not consider it in further discussion.

Recent experimental studies of the stability fields of these phases as a function of pressure, temperature, and f_{O_2} can be used to evaluate the most plausible oxides (36, 37). These studies point out that both Fe_4O_5 and Fe_5O_6 are stable phases over a

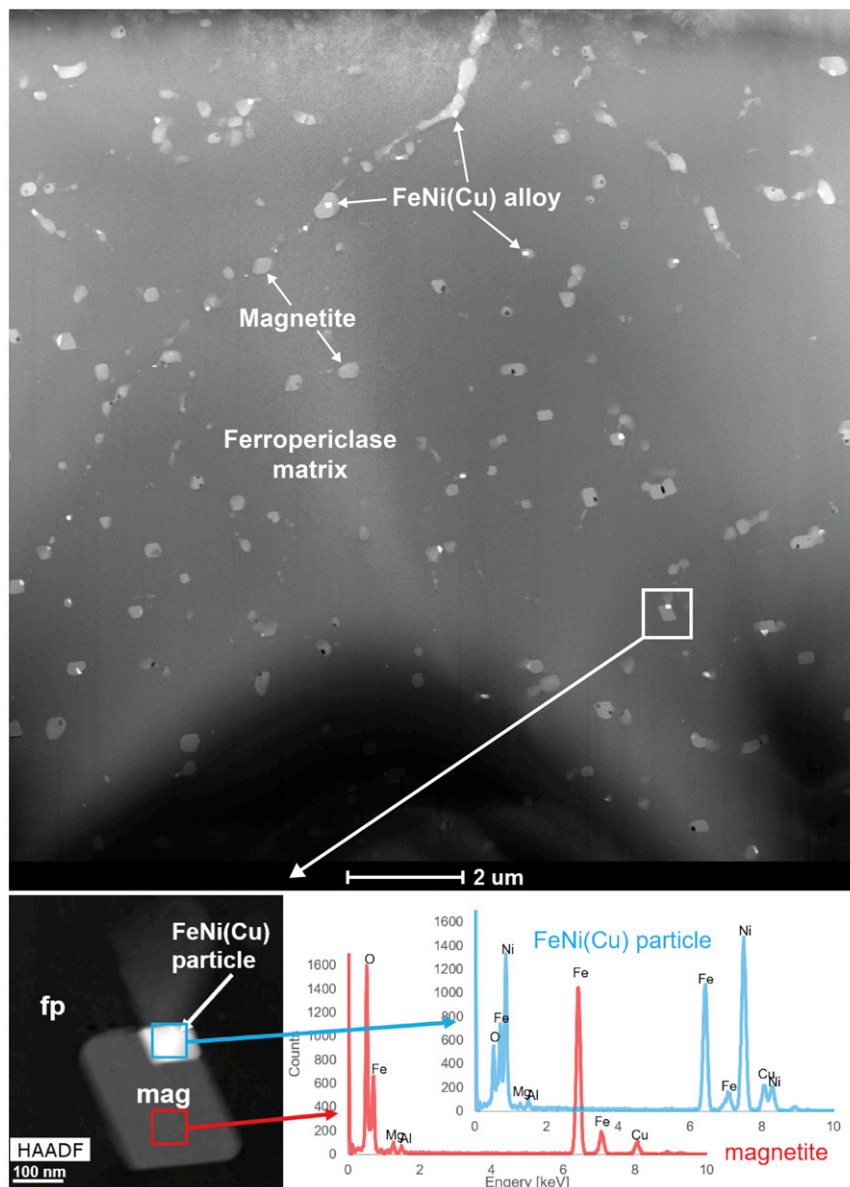


Fig. 2. HAADF-STEM image of sample AZ1_2 mounted on a copper TEM grid, showing Z contrast: brighter regions have a higher average atomic number, while darker regions have a lower average atomic number. The dark matrix is ferropericlasite, whereas gray grains represent magnetite. Bright spots are FeNi(Cu) particles. The original spectra are deconvolved and background corrected; the display is not quantitative.

wide range of conditions, from upper to lower mantle. At the minimum P - T conditions of crystallization of the ferropericlasite investigated here [i.e., $15.7 (\pm 2.5)$ GPa at $1,830 (\pm 45)$ K, ref. 26], both experimental studies support the stability of Fe_4O_5 relative to Fe_5O_6 , irrespective of the initial Fe content (37) and the Fe/Mg (36) of the bulk rock. The possibility that Fe_4O_5 is an oxide originally exsolved from ferropericlasite is further supported by f_{O_2} calculations. The stability of Fe_4O_5 would require f_{O_2} at least above the enstatite + magnetite = wadsleyite + diamond buffer by ~ 2 log units, which is above the f_{O_2} at which diamond and carbonate coexist along with clinoenstatite and wadsleyite (12, 36). Such oxidized conditions are not surprising as they have been invoked to explain the variability of Fe# in natural ferropericlasite (20, 27) and the incorporation of Fe^{3+} in ferropericlasite (44) and are more oxidized than those at which elemental Fe would be stable (i.e., below the iron-wüstite buffer). The formation of Fe_4O_5 would thus be a direct consequence of the oxidation of ferropericlasite, a natural carrier of ferric iron.

We thus propose that ferropericlasite first formed and was trapped as a single phase during the growth of the diamond (i.e., as a syngenetic inclusion) by redox reactions with the surrounding C-O(-H) fluid (6, 20, 24). In the presence of carbonated fluids, the f_{O_2} must have been such that ferropericlasite oxidized to incorporate relatively high Fe^{3+} contents [~ 2 – 10% is a reasonable range from literature data (12, 25, 44, 45)]. The exsolution of an Fe^{3+} -rich iron oxide then occurred due to a decrease in the solubility of Fe^{3+} in ferropericlasite as the conditions changed. At room pressure and 1,273 K the $\text{Fe}^{3+}/\sum\text{Fe}$ ratio of $(\text{Mg}_{0.8}\text{Fe}_{0.2})\text{O}$ reaches a maximum of $\sim 44\%$ at an f_{O_2} where it coexists with magnesioferrite (46). This maximum level of Fe^{3+} solubility, however, decreases with MgO content, pressure, and temperature. For a ferropericlasite with a nominal composition of $(\text{Mg}_{0.60}\text{Fe}_{0.40})\text{O}$, room-pressure data imply a maximum $\text{Fe}^{3+}/\sum\text{Fe}_{\text{tot}}$ ratio closer to 25% (47). The formation at pressures above 8 GPa of iron oxides with stoichiometries that

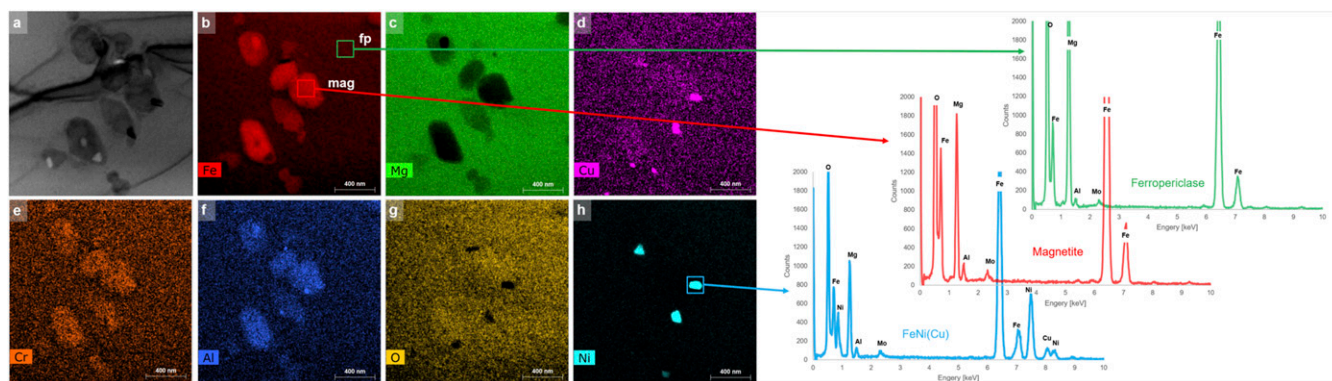


Fig. 3. Element distribution maps in the ferropiclasite (fp), magnetite (mag), and FeNi(Cu) particles on sample AZ1_1B mounted on a molybdenum TEM grid. (A) Bright-field micrograph. (B–H) Element distributions of the elements indicated in the lower-left corner of each panel; the original spectra are deconvoluted and background corrected and the display is not quantitative. Note the spatially positively correlated distribution of Fe–Al–Cr inversely correlated to Mg, while the distribution of Cu and Ni is in places positively correlated or not at all correlated.

lie between wüstite and magnetite should result in lower $\text{Fe}^{3+}/\sum\text{Fe}_{\text{tot}}$ ratios in wüstite and ferropiclasite because the stability fields of the high-pressure oxides extend to lower oxygen fugacities compared to magnetite (36). High-pressure experiments also seem to indicate generally lower ferropiclasite $\text{Fe}^{3+}/\sum\text{Fe}$ ratios at transition zone conditions. Ref. 46 for example determined an $\text{Fe}^{3+}/\sum\text{Fe}_{\text{tot}}$ ratio of 0.074 for $(\text{Mg}_{0.8}\text{Fe}_{0.2})\text{O}$ ferropiclasite at 18 GPa and 1273 K at an oxygen fugacity buffered by Re and ReO_2 , which should render an oxygen fugacity close to the solubility level (36).

Calculations indicate that at the entrapment pressure of the inclusion studied (which likely also partitioned Ni and Cu), Fe_4O_5 should be the phase that would exsolve once the ferropiclasite Fe^{3+} solubility limit was exceeded (36). The latter phase presumably also partitioned significant Ni and Cu as it formed. Below 8 GPa magnetite is experimentally demonstrated to be the stable phase (36, 37). In addition, magnetite lamellar intergrowths in Fe_4O_5 in samples recovered to ambient pressures have been reported (37). We interpret the final exsolution of the FeNi(Cu) metal alloy as having occurred subsequently as the

diamond cooled to temperatures <873 K where the Fe_4O_5 (possibly but not necessarily coexisting with magnetite) became unstable (48). The decompression and cooling of the diamond must have occurred rapidly because of the apparent insufficient time for the high-pressure iron oxide to reequilibrate with the surrounding ferropiclasite after. Current estimates of the ascent rate of CO_2 -rich magmas, which are candidates to carry diamond samples from the mantle to the surface, are in the range of $300\text{--}1,850\text{ m}\cdot\text{y}^{-1}$ becoming eventually faster as these melts start channeling (49).

In this study, nanometric textural observations along with quantitative chemical and structural analyses lead to the identification of inclusions that appear to have grown through a multistage process, starting with the entrapment of a single Fe^{3+} -bearing ferropiclasite inclusion. After entrapment the exsolution of a high-pressure mixed-valence iron oxide, most likely Fe_4O_5 , occurred as a result of changing conditions leading to a decrease in the Fe^{3+} solubility in ferropiclasite. Fe_4O_5 , therefore, would form through the reaction

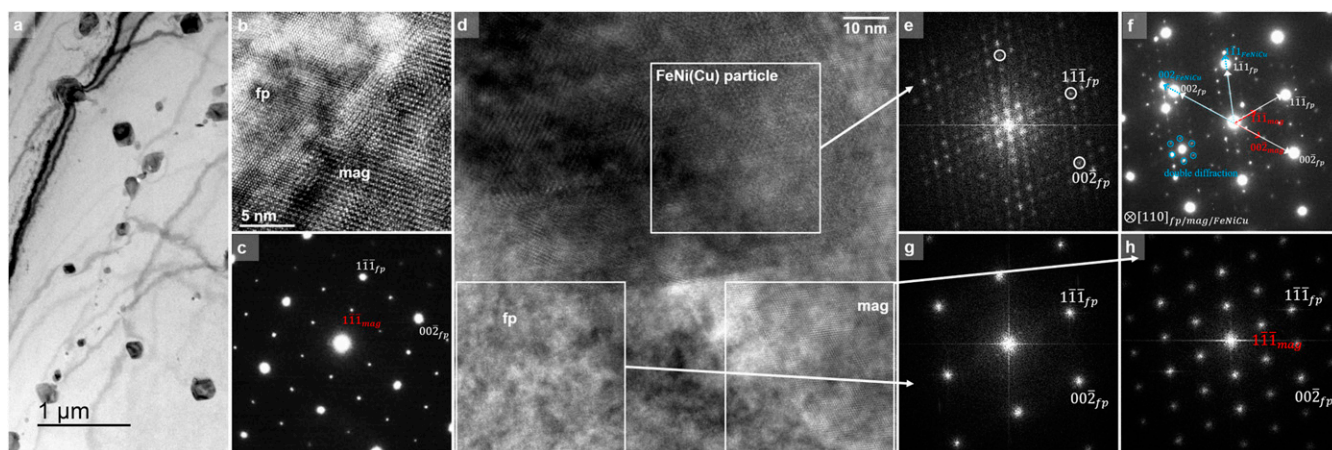
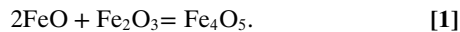
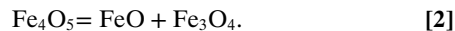


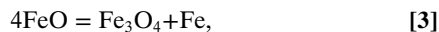
Fig. 4. Overview of the orientation relationships between fp, mag, and the FeNi(Cu) particles. (A) Bright field of the general distribution of magnetite in ferropiclasite. The magnetite exsolution often aligned along trails or chains. (B) HRTEM. Ferropiclasite in the upper-left corner and magnetite in the lower-right corner. (C) Selected area diffraction pattern of fp and mag. The well-known topotaxy is revealed (the general direction $\{111\}$ mag parallel $\{111\}$ fp). (D) HRTEM of a relatively thick region containing fp, mag, and an FeNi(Cu) particle. (E, G, and H) Fourier transformations of the indicated regions, while F is a selected area diffraction pattern of the whole region. The primary diffraction peaks are identified as fp (white arrows), mag (red arrows), and FeNi(Cu) (blue arrows). The additional peaks that belong to neither fp, mag, nor FeNi(Cu) arise from double diffraction. The primary electron beam is rediffracted by the small-sized FeNi(Cu) and magnetite particle; they are exemplarily indicated in blue. They repeat around many primary diffraction peaks. Note the streaks in the $(1\bar{1}1)$ reciprocal direction associated with the 002 FeNi(Cu) reflection.



An increase in f_{O_2} is unlikely to have caused this exsolution once the inclusion was trapped within the diamond. Potential causes are thus either an increase in pressure or a decrease in temperature (29, 46–48). Upon decompression below 8 GPa, Fe_4O_5 decomposes to wüstite and magnetite (36) as follows:



On further cooling toward room temperature after emplacement in the crust, wüstite becomes unstable and metallic Fe(Ni) forms through the reaction (48)



with nickel and other siderophile elements also partitioning into the metallic phase.

Earlier studies (18, 20, 22–25) have identified the phase that exsolved from ferropericlasite inclusions as magnesioferrite. However, there is no clear mechanism through which metal should form from magnesioferrite without reducing the f_{O_2} , which seems unlikely once the inclusion is trapped. Because these are physically isolated from the rocks surrounding the diamond crystals, we propose that the metal forms as decomposition product of Fe_4O_5 during decompression.

In conclusion, we investigated an Fe^{3+} -bearing ferropericlasite inclusion trapped in a superdeep diamond that shows FeNi(Cu) metallic particles in close spatial relation with nearly pure magnetite grains. These observations can be explained by: 1) formation of Fe_4O_5 by exsolution upon cooling; 2) decomposition of Fe_4O_5 into wüstite and magnetite; and 3) further exsolution of an FeNi(Cu) metal alloy (Fig. 1). The previously unknown petrological process documented here may also be applicable to the interpretation of certain xenolith suites, such as pyroxene-ilmenite intergrowths sampled from kimberlites, as these form by decompression exsolution from lower-mantle Ca–Ti–Si perovskite (50). This study calls for detailed further investigations of ferropericlasite inclusions in other such diamond samples where either the presence of magnetite and/or magnesioferrite has been reported as potential residual of Fe_xO_y phases. Finding additional examples with the features observed in our sample will not only further clarify the origin of the Fe_xO_y phases, but also shed light on previously unobserved petrological deep-Earth processes.

Materials and Methods

Sample. The diamond investigated in this study (Fig. 1A) was a flattened colorless dodecahedron recovered from alluvial deposits of the São Luiz River, in the Juina area of Mato Grosso State, Brazil (see also refs. 17 and 18). The sample contained two main black tabular inclusions, identified as ferropericlasite $[(\text{Mg}_{0.60}\text{Fe}_{0.40})\text{O}]$ by single-crystal X-ray diffraction. The longest dimension of the smaller inclusion (AZ1_1) was $\sim 160 \mu\text{m}$, whereas that of the larger inclusion (AZ1_2) was $\sim 340 \mu\text{m}$. Additional study of the diamond host and the two inclusions has been reported in ref. 26.

1. T. Stachel, J. W. Harris, The origin of cratonic diamonds—Constraints from mineral inclusions. *Ore Geol. Rev.* **34**, 5–32 (2008).
2. M. J. Walter *et al.*, Deep mantle cycling of oceanic crust: Evidence from diamonds and their mineral inclusions. *Science* **334**, 54–57 (2011).
3. D. G. Pearson *et al.*, Hydrous mantle transition zone indicated by ringwoodite included within diamond. *Nature* **507**, 221–224 (2014).
4. E. M. Smith *et al.*, Large gem diamonds from metallic liquid in Earth's deep mantle. *Science* **354**, 1403–1405 (2016).
5. F. Nestola *et al.*, CaSiO_3 perovskite in diamond indicates the recycling of oceanic crust into the lower mantle. *Nature* **555**, 237–241 (2018).
6. A. R. Thomson, M. J. Walter, S. C. Kohn, R. A. Brooker, Slab melting as a barrier to deep carbon subduction. *Nature* **529**, 76–79 (2016).
7. E. M. Smith *et al.*, Blue boron-bearing diamonds from Earth's lower mantle. *Nature* **560**, 84–87 (2018).
8. O. Tschauer *et al.*, Ice-VII inclusions in diamonds: Evidence for aqueous fluid in Earth's deep mantle. *Science* **359**, 1136–1139 (2018).

SEM. The two ferropericlasite inclusions were first extracted by mechanical crushing of the host, then polished in a three-step process and finally carbon coated. FEG-SEM measurements were carried out at the Department of Physics and Astronomy (University of Padova), using a Zeiss SIGMA HD FEG-SEM microscope operating at 20 kV, with a spot size of $\sim 1 \text{ nm}$. Imaging was performed using an InLens secondary electron detector. Compositional analysis was performed using an EDS (Oxford Instruments). The spatial resolution in microanalysis was of $\sim 1 \mu\text{m}$.

EMPA. Chemical analyses were carried out using a CAMECA SX50 electron microprobe at the Electron Microprobe Laboratory of the Institute of Geosciences and Earth Resources—National Research Council of Italy, hosted by the Department of Geosciences of University of Padova. The analyses were conducted using wavelength-dispersive spectroscopy and an accelerating voltage of 20 kV, probe beam current of 20 nA, and a 2- μm beam diameter. Standards (analyzer crystal, element, emission line) used were MgO (TAP, MgK α); diopside (TAP, SiK α); Al_2O_3 (TAP, AlK α); MnTiO_3 (LIF, MnK α); Cr_2O_3 (LIF, CrK α); Fe_2O_3 (LIF, FeK α); NiO (LIF, NiK α); and Cu (LIF, CuK α). We have collected 39 chemical analyses over the AZ_1 inclusion. Analytical data are reported in *SI Appendix, Table S1*.

TEM. Samples for TEM were prepared using the FEI Scios dual-beam device at Bayerisches Geoinstitut (BGI, University of Bayreuth). The lamellae were cut specifically from locations previously identified in the FEG-SEM. Note that samples AZ1_1A and AZ1_2 were attached to an Omniprobe Cu-grid, while sample AZ1_1B (on which we collected the data shown in Fig. 3) was mounted on a Mo grid in order to discriminate the real presence of Cu. An FEI Titan G2 80–200 microscope at BGI was used for nanometer-scale characterization. We combined conventional TEM, high-resolution (HR)-TEM as well as scanning (S)-TEM modes. The acceleration voltage was set to 200 kV; EDS analyses were performed in STEM mode. The probe size after careful optimization is 160 PM, and the final image resolution is a convolution of pixel and probe size. For imaging we acquired BF, ADF, and HAADF signals. The HAADF was optimized to yield Z contrast. EDS spectra were acquired using a windowless SuperX-EDS detector with four Si-drift detectors inclined toward the sample in a superimposed circle, resulting in 0.7 sr solid angle, and pixel sizes of 2 nm.

Data Availability Statement. EMPA data have been deposited in the Research Data Unipd data archive at DOI: [10.25430/researchdata.cab.unipd.it.00000358](https://doi.org/10.25430/researchdata.cab.unipd.it.00000358). All other data are included in the article and *SI Appendix*.

ACKNOWLEDGMENTS. This investigation was financially supported by the project INDIMEDEA (“Inclusions in Diamonds: Messengers from the Deep Earth”), funded by a European Research Council Starting Grant 2012 to F.N. (Grant 307322). C.A. acknowledges financial support through a Canada Excellence Research Chair grant to D.G.P. and the Diamond Exploration and Research Training School. K.M. acknowledges financial support through Grants MA6287/3 and MA6287/6 of the German Science Foundation. V.S. acknowledges financial support through “Fondi di Ateneo 2017 and 2018.” L.B. thanks the Italian Ministry of Education, University and Research, project “TEOREM deciphering geological processes using Terrestrial and Extraterrestrial ORE Minerals” (Prot. 2017AK8C32). R.J.H. acknowledges support of the A. F. Sloan Foundation through the Deep Carbon Observatory. L. Tauro and N. Michieli are acknowledged for their help in the FEG-SEM sample preparation and analysis, respectively. We are grateful to D. Wiesner and J. Polednia for FIB sample preparation. FEI Scios FIB machine, BGI Bayreuth, is supported through Grant INST 91/315-1 FUGG. We thank R. Carampin for providing technical assistance in the EMPA analyses, S. Castelli for the photograph of the diamond in Fig. 1, and the DeBeers Group of Companies for the donation of the diamond to J.W.H.

9. D. P. Araujo, J. C. Gaspar, Y. Fei, E. Hauri, R. J. Hemley, Mineralogy of diamonds from the Juina kimberlite province, SW Amazon Craton, Brazil: Cathodoluminescence, infrared spectroscopy, nitrogen content, and carbon and nitrogen isotopes. *Rev. Bras. Geocienc.* **31**, 669–671 (2001).
10. D. J. Frost *et al.*, Experimental evidence for the existence of iron-rich metal in the Earth's lower mantle. *Nature* **428**, 409–412 (2004).
11. M. J. Walter *et al.*, Primary carbonatite melt from deeply subducted oceanic crust. *Nature* **454**, 622–625 (2008).
12. V. Stagno *et al.*, The stability of magnesite in the transition zone and the lower mantle as function of oxygen fugacity. *Geophys. Res. Lett.* **38**, L19309 (2011).
13. F. Kaminsky, Mineralogy of the lower mantle: A review of “super-deep” mineral inclusions in diamond. *Earth Sci. Rev.* **110**, 127–147 (2012).
14. V. Stagno, Carbon, carbides, carbonates and carbonatitic melts in the Earth's interior. *J. Geol. Soc. London* **176**, 375–387 (2019).
15. V. Stagno *et al.*, “Carbon-bearing phases throughout Earth's interior;” in *Deep Carbon*, (Cambridge University Press, 2019), pp. 66–88.

16. L. Stixrude, C. Lithgow-Bertelloni, Geophysics of chemical heterogeneity in the mantle. *Annu. Rev. Earth Planet. Sci.* **40**, 569–595 (2012).
17. P. C. Hayman, M. G. Kopylova, F. V. Kaminsky, Lower mantle diamonds from Rio Soriso (Juina area, Mato Grosso, Brazil). *Contrib. Mineral. Petrol.* **149**, 430–445 (2005).
18. B. Harte, J. W. Harris, M. T. Hutchison, G. R. Watt, M. C. Wilding, "Lower mantle mineral associations in diamonds from Sao Luiz, Brazil" in *Mantle Petrology: Field Observations and High-Pressure Experimentation: A Tribute to Francis R. (Joe) Boyd*, (The Geological Society, 1999), Vol. 6, pp. 125–153.
19. L.-G. Liu, An alternative interpretation of lower mantle mineral associations in diamonds. *Contrib. Mineral. Petrol.* **144**, 16–21 (2002).
20. P. Nimis *et al.*, Fe-rich ferropervicite and magnesio-wüstite inclusions reflecting diamond formation rather than ambient mantle. *Geology* **47**, 27–30 (2019).
21. F. Zhu *et al.*, Kinetic control on the depth distribution of superdeep diamonds. *Geophys. Res. Lett.* **46**, 1984–1992 (2019).
22. R. Wirth, L. Dobrzynetskaya, B. Harte, A. Schreiber, H. W. Green, High-Fe (Mg, Fe)O inclusion in diamond apparently from the lowermost mantle. *Earth Planet. Sci. Lett.* **404**, 365–375 (2014).
23. F. V. Kaminsky *et al.*, Oxidation potential in the Earth's lower mantle as recorded by ferropervicite inclusions in diamond. *Earth Planet. Sci. Lett.* **417**, 49–56 (2015).
24. M. Palot *et al.*, Evidence for H₂O-bearing fluids in the lower mantle from diamond inclusion. *Lithos* **265**, 237–243 (2016).
25. F. Nestola *et al.*, Synchrotron Mössbauer source technique for in situ measurement of iron-bearing inclusions in natural diamonds. *Lithos* **265**, 328–333 (2016).
26. C. Anzolini *et al.*, Depth of diamond formation obtained from single periclavite inclusions. *Geology* **47**, 219–222 (2019).
27. F. V. Kaminsky, R. Wirth, A. Schreiber, A microinclusion of lower-mantle rock and other mineral and nitrogen lower-mantle inclusions in a diamond. *Can. Mineral.* **53**, 83–104 (2015).
28. D. Nishio-Hamane, Fe³⁺ and Al solubilities in MgSiO₃ perovskite: Implication of the Fe³⁺AlO₃ substitution in MgSiO₃ perovskite at the lower mantle condition. *Geophys. Res. Lett.* **32**, L16306 (2005).
29. M. Longo, C. A. McCammon, S. D. Jacobsen, Microanalysis of the iron oxidation state in (Mg,Fe)O and application to the study of microscale processes. *Contrib. Mineral. Petrol.* **162**, 1249–1257 (2011).
30. B. Lavina *et al.*, Discovery of the recoverable high-pressure iron oxide Fe₄O₅. *Proc. Natl. Acad. Sci. U.S.A.* **108**, 17281–17285 (2011).
31. A. B. Woodland, D. J. Frost, D. M. Trots, K. Klimm, M. Mezouar, In situ observation of the breakdown of magnetite (Fe₃O₄) to Fe₄O₅ and hematite at high pressures and temperatures. *Am. Mineral.* **97**, 1808–1811 (2012).
32. B. Lavina, Y. Meng, Unraveling the complexity of iron oxides at high pressure and temperature: Synthesis of Fe₅O₆. *Sci. Adv.* **1**, e1400260 (2015).
33. R. Sinmyo *et al.*, Discovery of Fe₇O₈: A new iron oxide with a complex monoclinic structure. *Sci. Rep.* **6**, 32852 (2016).
34. T. Ishii, L. Uenver-Thiele, A. B. Woodland, E. Alig, T. Boffa Ballaran, Synthesis and crystal structure of Mg-bearing Fe₃O₁₁: New insight in the complexity of Fe-Mg oxides at conditions of the deep upper mantle. *Am. Mineral.* **103**, 1873–1876 (2018).
35. A. B. Woodland *et al.*, Fe₄O₅ and its solid solutions in several simple systems. *Contrib. Mineral. Petrol.* **166**, 1677–1686 (2013).
36. R. Myhill *et al.*, On the P–T–f_{O₂} stability of Fe₄O₅, Fe₅O₆ and Fe₄O₅-rich solid solutions. *Contrib. Mineral. Petrol.* **171**, 51 (2016).
37. K. Hikosaka, R. Sinmyo, K. Hirose, T. Ishii, Y. Ohishi, The stability of Fe₅O₆ and Fe₄O₅ at high pressure and temperature. *Am. Mineral.* **104**, 1356–1359 (2019).
38. C. Ballhaus, Is the upper mantle metal-saturated? *Earth Planet. Sci. Lett.* **132**, 75–86 (1995).
39. A. Rohrbach *et al.*, Metal saturation in the upper mantle. *Nature* **449**, 456–458 (2007).
40. A. Rohrbach, M. W. Schmidt, Redox freezing and melting in the Earth's deep mantle resulting from carbon-iron redox coupling. *Nature* **472**, 209–212 (2011).
41. A. Rohrbach, S. Ghosh, M. W. Schmidt, C. H. Wijbrans, S. Klemme, The stability of Fe–Ni carbides in the Earth's mantle: Evidence for a low Fe–Ni–C melt fraction in the deep mantle. *Earth Planet. Sci. Lett.* **388**, 211–221 (2014).
42. D. J. Frost, C. A. McCammon, The redox state of Earth's mantle. *Annu. Rev. Earth Planet. Sci.* **36**, 389–420 (2008).
43. A.-L. Auzende *et al.*, Element partitioning between magnesium silicate perovskite and ferropervicite: New insights into bulk lower-mantle geochemistry. *Earth Planet. Sci. Lett.* **269**, 164–174 (2008).
44. K. Otsuka, M. Longo, C. A. McCammon, S.-I. Karato, Ferric iron content of ferropervicite as a function of composition, oxygen fugacity, temperature and pressure: Implications for redox conditions during diamond formation in the lower mantle. *Earth Planet. Sci. Lett.* **365**, 7–16 (2013).
45. C. A. McCammon, T. Stachel, J. W. Harris, Iron oxidation state in lower mantle mineral assemblages. *Earth Planet. Sci. Lett.* **222**, 423–434 (2004).
46. C. McCammon, J. Peyronneau, J.-P. Poirier, Low ferric iron content of (Mg,Fe)O at high pressures and temperatures. *Geophys. Res. Lett.* **25**, 1589–1592 (1998).
47. D. H. Speidel, Phase equilibria in the system MgO-FeO-Fe₂O₃: The 1300 °C isothermal section and extrapolations to other temperatures. *J. Am. Ceram. Soc.* **50**, 243–248 (1967).
48. B. Sundman, An assessment of the Fe-O system. *J. Phase Equilibria* **12**, 127–140 (1991).
49. V. Stagno, V. Stopponi, Y. Kono, C. E. Manning, T. Irifune, Experimental determination of the viscosity of Na₂CO₃ melt between 1.7 and 4.6 GPa at 1200–1700 °C: Implications for the rheology of carbonatite magmas in the Earth's upper mantle. *Chem. Geol.* **501**, 19–25 (2018).
50. K. D. Collerson, H. Terasaki, E. Ohtani, A. Suzuki, T. Kondo, "A lower mantle origin for megacryst suite pyroxene-ilmenite xenoliths in kimberlites: High-pressure experimental constraints and geodynamic significance" in *EOS Transactions of the American Geophysical Union*, (American Geophysical Union, 2004), Vol. 85.